Hindawi
International Journal of Antennas and Propagation
Volume 2020, Article ID 9243609, 18 pages
https://doi.org/10.1155/2020/9243609

Research Article

Design and Analysis of Antenna Feeding Networks Based on the Rotman Lens Using Interval Analysis (IA)

Massimo Donelli and Mohammedhusen H. Manekiya

Department of Electronics and Communication Engineering, University of Trento, Trento 38123, Italy

Correspondence should be addressed to Massimo Donelli; massimo.donelli@unitn.it

Received 23 October 2019; Revised 3 January 2020; Accepted 30 January 2020; Published 5 March 2020

Academic Editor: Renato Cicchetti

A new method for the design of antenna array feeding networks has been proposed in this work. In particular, the considered feeding networks are based on the Rotman lens. By knowing the maximum errors on the fabrication tolerances, the arithmetic of intervals and interval analysis (IA) are used for determining the lower and upper bounds of the antenna feeding network parameters of interest. Representative and preliminary numerical results are reported to show the potentialities of the proposed method. An experimental X-band Rotman lens prototype has been designed, fabricated, and assessed. The obtained results are quite good.

1. Introduction

Modern telecommunication systems such as mobile smartphones offer multimedia applications and different services that require high reconfigurability despite the limited dimensions of the devices. 5G and 4G generation devices offer, in addition to usual voice and other services commonly provided by standard 3G systems, ultra-broadband Internet connection, voice-over telephony (VOIP), mobile web access, gaming services, and other exciting multimedia applications (such as a high-definition television). The use of advanced RF techniques such as MIMO antennas, multiband antenna and feeding networks, and carrier aggregation (CA) could actively improve the performances of the standard radar or radio links. In such a framework, the design of a suitable radiating system and feeding networks can play a vital role in the design of new-generation communication devices. The antenna systems and the related feeding networks for these new devices need to be light, cheap, and able to keep device performances at a high level. This results in RF devices with high complexity and in challenging RF requirements, especially on the antenna feeding network.

In the last decades, the use of reconfigurable antenna arrays with fully adaptive properties [1–6] clearly demonstrated their effectiveness to improve the performance of a telecommunication system dramatically. This kind of antenna, commonly used in several fields such as airport surveillance and missile detection and tracking, is unfortunately very complex, expensive, and bulky to be used for commercial portable devices such as mobile phones and tablets. Moreover, the introduction of new frequency bands that belong to the millimetric wavelength results in a dramatic increase of the feeding network components such as variable attenuators and phase shifters. For low-cost applications, the use of switched beam antennas is generally adopted instead of adaptive arrays. Recently, a new kind of reconfigurable parasitic antenna, able to electronically select different configurations of the radiation patterns [7–9], has been successfully adopted for various practical applications, such as Wi-Fi systems [10], wireless sensor network applications [11], and sum-difference radar [12]. These antennas offer a good compromise between fully adaptive arrays and the switched beam solution, but the complexity of the feeding network is still too complex or expensive. The Rotman lens has proven its capability to be a useful beamformer for designers of electronically scanned arrays [13–19]. It is particularly helpful for the design of multibeam or reconfigurable arrays because it offers a real-time delay phase shift capability that is independent of frequency and

removes the need for expensive phase shifters to steer a beam over wide angles. The Rotman lens has a long history in communication systems ranging from military radar up to standard radio links [20]. The Rotman lens is a planar structure, which can be easily implemented with microstrip technology, and it is used to feed an antenna array to obtain a multibeam behaviour; since it does not require lumped elements or other RF devices, it is simple, cheap, and mechanically robust. Despite the simplicity of the design equations, they are not able to take into account all the real-world effects, such as the material or fabrication tolerances, which can actively reduce the performance of the Rotman lens and require an expensive experimental calibration tuning [21–31]. The proposed method in this paper is based on the use of the interval analysis (IA) and the interval arithmetic for the design of the Rotman lens. IA was initially introduced to bound rounding errors in numerical computations [32, 33], and it has been then extended to the solution of linear and nonlinear equations and functional optimisation [34, 35]. Nowadays, interval analysis is widely used in many engineering applications, but its applications to electromagnetics are still limited to few applications mainly concerned with the design of robust antennas [36] or microwave imaging applications [37–39]. In this work, the reliability of the IA is used to define an innovative design method where the Rotman lens design formulas are firstly reformulated within the interval arithmetic, and secondly, an IA-based refinement algorithm has to be applied to identify the lens parameters better. The outline of this paper is as follows: the problem of the Rotman lens design is mathematically formulated according to the principles of the arithmetic of intervals in Section 2, while Section 3 is dedicated to present the IA-based design methodology. A set of numerical experiments considering Rotman lenses in the S, C, and K bands is reported and discussed in Section 3.1 to show the effectiveness of the approach. Moreover, in Section 3.2, an experimental X-band Rotman lens prototype has been designed, fabricated, and assessed. Concluding remarks are drawn in Section 4, where innovative features and peculiarities of the proposed design method are also pointed out to encourage possible future improvements.

2. Mathematical Formulation

A Rotman lens is a feeding network made with a parallel plate structure. The shape is carefully chosen to produce a wavefront across the output ports, which connect the array elements that are phased by the time delay. A standard Rotman lens layout is shown in Figure 1: as it can be noticed, it consists of a parallel plate region surrounded by a number N_a of output ports, N_b input ports called beam ports, and some N_d dummy ports used to obtain reflection-less termination around the parallel plate region. The design of a Rotman lens starts with the definition of the number of radiating elements (N_a) and their location along the array axis, the number of beams, and the required beam steering angles. The other lens parameters are the focal angle α, the focal ratio $\beta = f_2/f_1$, and the expansion factor defined as $\gamma = \sin\theta/\sin\alpha$. The length of the transmission lines that connect the array elements located on the array axis must be

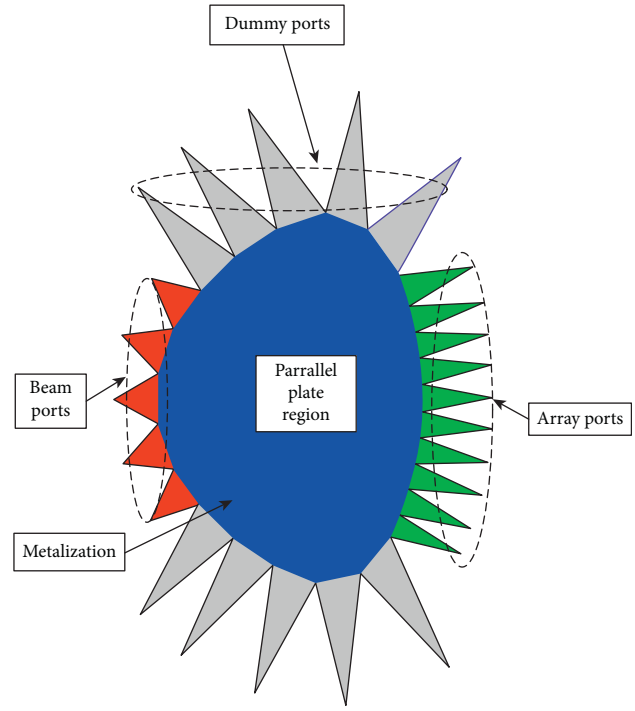

Figure 1: Rotman lens layout.

normalised with respect to the focal length f_1. These parameters are shown in Figure 2, where it can be seen that F_0, F_1, and F_2 are the three foci of the circular beam port arc (in these points, there are no phase errors), following the formulation reported in [19] and considering the interval arithmetic's rules [32]. The tolerances of the considered ceramic material Arlon 25N are $t = 0.5 \pm 0.07$ (mm), thickness of the metalization $t_m = 10 \pm 2$ (μm), and $\varepsilon_r = 3.28 \pm 0.05$. The mechanical tolerance of the CNC machine for the microstrip width, lens geometrical characteristics, tapered line structure, transmission line length, and antenna element dimensions is ± 0.05 (mm). Considering the above mechanical and electrical tolerances, the lens design formulas have been reformulated. A given interval is represented with a tilde as follows: $\tilde{\varepsilon} = [\inf\{\tilde{\varepsilon}\}; \sup\{\tilde{\varepsilon}\}]$, where $\inf\{\tilde{\varepsilon}\} = \varepsilon - \varepsilon^{(\inf)}$ and $\sup\{\tilde{\varepsilon}\} = \varepsilon + \varepsilon^{(\sup)}$. The array ports' phase centre locations $(\tilde{x}_n^{(ap)}, \tilde{y}_n^{(ap)})$, $n = 1, \ldots, N_a$, are provided by the following equations:

$$\tilde{x}_n^{(ap)} = 1 - \frac{1/2\tilde{\Upsilon}_n^2 \sin^2(\alpha) + (1-\tilde{\beta})\tilde{W}}{1-\tilde{\beta}\cos(\alpha)},$$
$$\tilde{y}_n^{(ap)} = \tilde{\Upsilon}_n\left(1 - \frac{\tilde{W}}{\tilde{\beta}}\right), \quad n = 1, \ldots, N_a. \tag{1}$$

With the knowledge on the array port positions, the solution of the following equation can provide the length of the transmission microstrips connected with the antenna elements (green lines in Figure 2):

$$\tilde{a}\tilde{w}^2 + \tilde{b}\tilde{w} + \tilde{c} = 0, \tag{2}$$

where $\tilde{w}_n = \tilde{W}_n/\tilde{f}_1\{n = 1, \ldots, N_a\}$ are the normalised lengths of the transmissions line connected with the antenna

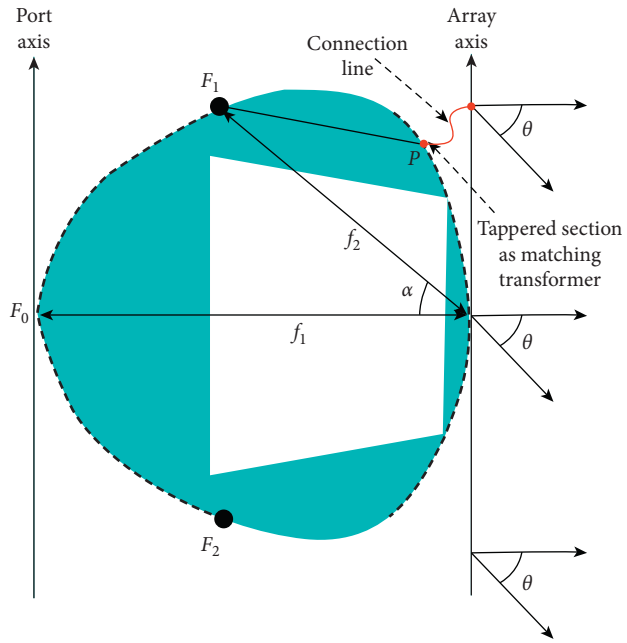

Figure 2: Rotman lens design geometry.

ports and the antenna elements. The coefficients $\tilde{a}$, $\tilde{b}$, and $\tilde{c}$ are defined as follows (see Appendix for more details):

$$\tilde{a} = 1 - \left(\frac{b_1}{b_0}\eta\right)^2 - \left(\frac{g-1}{g-a_0}\right)^2,$$

$$\tilde{b} = 2g\left(\frac{a_0-1}{g-a_0}\right) + \left(\frac{2}{b_0^2} - \frac{g-1}{(g-a_0)^2}\right)b_1^2\eta^2, \tag{3}$$

$$\tilde{c} = \frac{gb_1^2\eta^2}{g-a_0} + \frac{b_1^4\eta^4}{4(g-a_0)^2} - \left(\frac{b_1}{b_0}\eta\right)^2.$$

The solution of equation (2) provides the intervals of each transmission line length $\tilde{w}_n\{n = 1, \ldots, N_a\}$. The locations of the beam ports $(\tilde{x}_m^{(bp)}, \tilde{y}_m^{(bp)}), m = 1, \ldots, N_b$, aimed at steering the main beam towards θ_m, $m = 1, \ldots, N_b$, can be estimated considering the following relations:

$$\begin{aligned} \tilde{x}_m^{(bp)} &= \tilde{\vartheta}(1 - \cos(\chi_m + \tilde{\varphi})), \\ \tilde{y}_m^{(bp)} &= \tilde{\vartheta}(\cos(\chi_m + \tilde{\varphi})), \quad m = 1, \ldots, N_b, \end{aligned} \tag{4}$$

where

$$\tilde{\vartheta} = 1 - \frac{\left(1 - \tilde{\beta}^2\right)}{2(1 - \tilde{\beta}\cos(\alpha))},$$

$$\chi_m = \sin^{-1}\left(\frac{\sin(\theta_m)}{\gamma}\right), \tag{5}$$

$$\tilde{\varphi} = \sin^{-1}\left(\frac{1-\tilde{\vartheta}}{\tilde{\vartheta}}\right).$$

The above formulas allow estimating the geometrical layout of the lens, while the following one allows determining the coupling terms between the N_b and the N_a beam and array ports:

$$\tilde{S}_{m,n} = \frac{\sin((k\tilde{w}_m/2)(\sin(\phi_m)))}{(k\tilde{w}_m/2)(\sin(\phi_m))} \frac{\sin((k\tilde{w}_n/2)(\sin(\phi_n)))}{(k\tilde{w}_n/2)s(in(\phi_n))} * \sqrt{\frac{\tilde{w}_m\tilde{w}_n}{\tilde{\lambda}\tilde{d}}} e^{-j(k\tilde{d}+\pi/4)}, \tag{6}$$

where $k = 2\pi/\tilde{\lambda}$ is the interval of the wavenumber in the dielectric substrate, $\tilde{d}$ is the interval of the interelement distance between the array elements, $\tilde{w}_n$ and $\tilde{w}_m$ are the intervals of the beam and array widths, respectively, and ϕ_n and ϕ_m are two angles measured considering the ports' boresight direction and the segment connecting the phase centres of the ports m and n. Equation (6) provides a prediction of fundamental antenna parameters such as the array factor, phase error, and illumination amplitudes. Equations (1)–(6) give all information needed for the geometrical structure of the Rotman lens as intervals; to obtain a better refinement of the interval estimation, the Skelboe–Moore algorithm [32] has been used. It is worth noticing that, after the design of a Rotman lens, often a manual tuning or an optimisation phase is mandatory to obtain the required performance and move towards the fabrication of an experimental prototype. The proposed method based on the interval arithmetic permits to avoid the time-consuming tuning phase and provides the lens geometrical parameters able to take into account the tolerances of materials and to guarantee the initial design requirements.

3. Numerical and Experimental Assessment

The proposed design method is assessed by reporting and discussing a selected set of representative results of numerical simulations in the following sections. All the numerical simulations have been carried out by considering a ceramic substrate Arlon 25N of 0.5 mm thickness with dielectric permittivity $\varepsilon_r = 3.28$ and $\tan(\delta) = 10^{-3}$. Numerical data from the obtained experimental prototype operating in the X band (8 – 12 GHz) have been designed, fabricated, and assessed.

3.1. Numerical Assessment. In the first experiment, an S-band (2 – 4 GHz) Rotman lens has been considered. The lens parameters are four beam ports with a scan angle of ± 25 degrees and centre frequency $f_c = 2.45$ GHz, sixteen array ports, and four dummy ports. The S-band lens is characterised with a focal length $f_1 = 5.5\lambda$, a focal angle $\alpha = 25$ (degrees), a focal ratio $\tilde{\beta} = f_2/f_1 = 0.9$, and an expansion factor $\gamma = 1$. The port impedance is 50 (Ω). All ports are connected with tapered transmission lines aligned towards the lens centre. The tapered line length, aimed at guaranteeing a good impedance matching and a phase error reduction, is represented as $L_t = 1\lambda$, while the beam and array ports are connected with microstrip lines of length $L_m = 0.5\lambda$. The S-band Rotman lens geometry is obtained

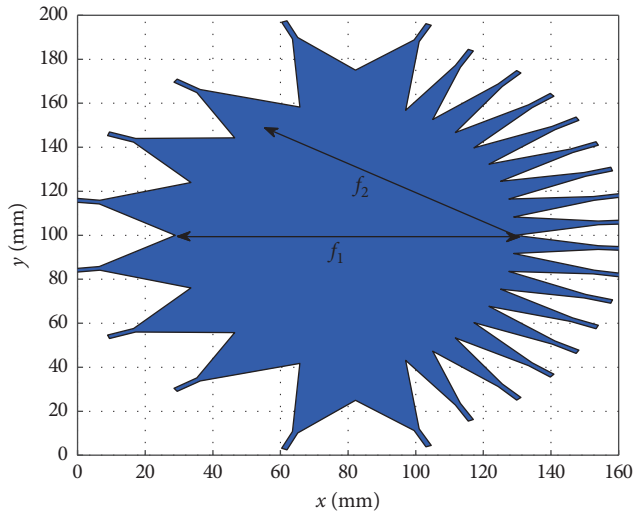

Figure 3: S-band Rotman lens port positions and position tolerances after IA refinement.

after the application of the design formulas (3)–(5) and the Skelboe–Moore refinement algorithm [32]. In particular, the beam, array, and dummy port positions are shown in Figure 3. All the port positions are reported considering the intervals of confidences provided by the upper and lower limits. The geometry layout of the S-band Rotman lens is reported in Figure 4.

To assess the S-band lens performance, the return loss S_{11} at the input beam ports has been estimated. In particular, the return loss vs. frequency has been measured in the range between 2.0 GHz and 3.0 GHz. The results are reported in Figure 5; as it can be noticed, the obtained results are quite satisfactory and the return loss is always in the range $-14\,\text{dB} < S_{11} < -18\,\text{dB}$. The isolation between the input ports is estimated in Figures 6(a) and 6(b); in particular, Figure 6(a) reports the isolation between two adjacent ports P1 and P2, while Figure 6(b) reports the isolation between two distant ports P1 and P4. As it can be noticed from the data reported in Figure 6, the isolation is very good: below −20 dB for the adjacent ports P1 and P2 and −30 dB for the distant ports P1 and P4. To show the focusing efficacy of the lens, the surface current flowing from the beam port P1 to the ten array ports P13, P14, . . ., P22 is reported in Figure 7. Finally, the phase errors measured at the ten array ports P13, P14, . . ., P22 are reported in Figure 8; as expected, the maximum phase error is measured at the ports P13 and P22 placed at the ends of the lens. However, the maximum phase error is below 1.5 degrees.

In the next experiment, a C-band (5 − 7 GHz) Rotman lens has been considered. Also in this experiment, four input beam ports with a scan angle of ± 25 degrees, ten array ports, and eight dummy ports have been considered. Also, in this case, the port impedance is 50 (Ω). The lens centre frequency is $f_c = 5.8$ GHz. Moreover, the other C-band geometrical parameters are the same as those in the previous example; in particular, focal length $f_1 = 5.5\lambda$, focal angle $\alpha = 25$ degrees, focal ratio $\widetilde{\beta} = f_2/f_1 = 0.9$, and expansion factor $\gamma = 1$. All ports are connected with tapered transmission lines of length $L_t = 1\lambda$, aligned towards

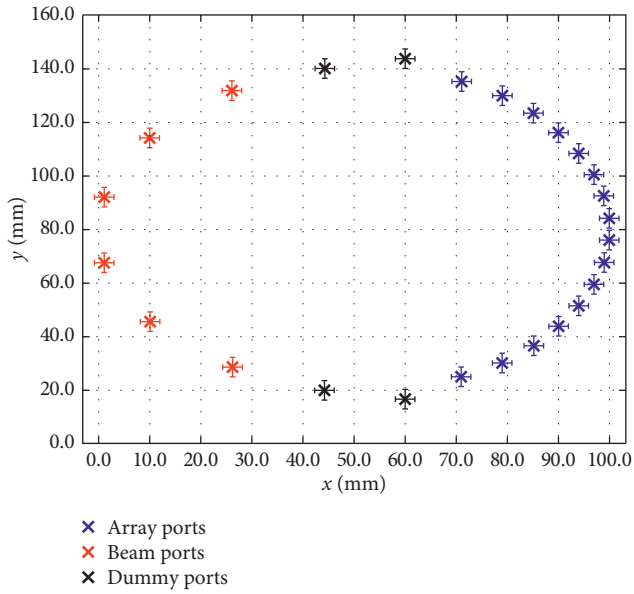

Figure 4: S-band Rotman lens geometry.

the lens centre, while the tapered microstrip lines that connect beam and array ports have a length of $L_m = 0.5\lambda$. The lens geometry and the positions of the ports have been obtained after the application of the design formulas (3)–(5) and the Skelboe–Moore refinement algorithm [32]. The port positions including the upper and lower limits provided by the IA analysis are shown in Figure 9, while the complete geometry of the C-band Rotman lens is reported in Figure 10.

The scattering parameters of the C-band prototype have been estimated; in particular, the return loss and the isolations at the input beam ports are reported in Figures 11 and 12.

The obtained results are quite good with a return loss in the range $-12\,\text{dB} > S_{11} > -22\,\text{dB}$, isolation between two adjacent ports P1 and P2 below −20 dB, and isolation below −29 dB for the more distant ports P1 and P4. The current

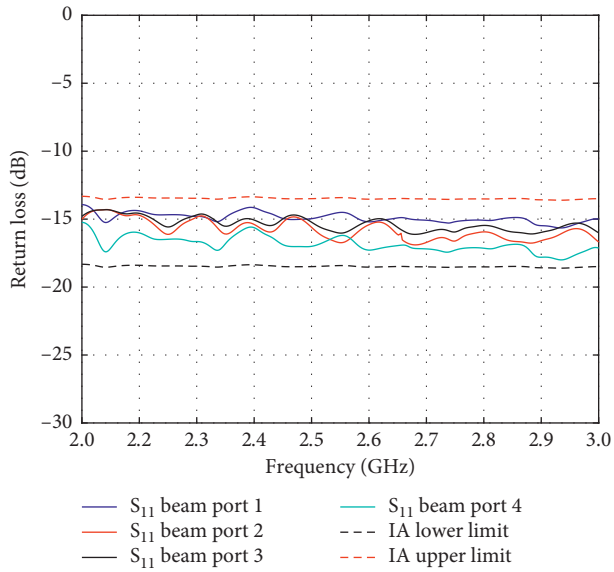

Figure 5: S-band Rotman lens: return loss at the beam ports.

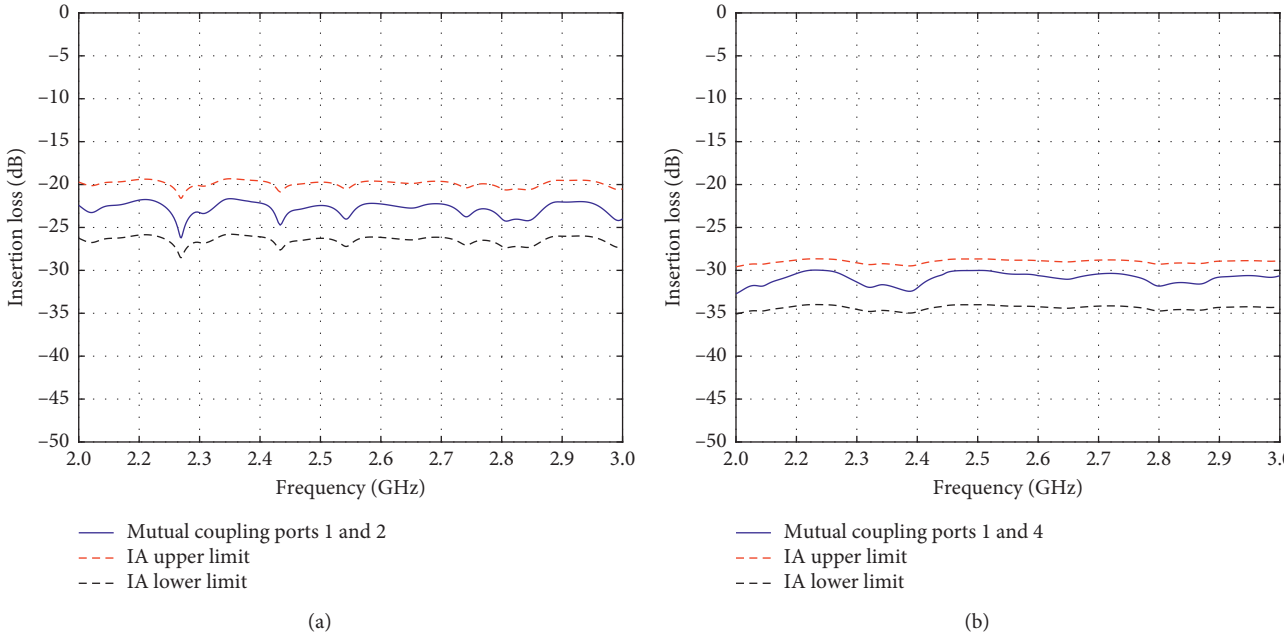

Figure 6: S-band Rotman lens: coupling factor vs. frequency (a) between ports P1 and P2 and (b) between ports P1 and P4.

distribution flowing from beam port P4 towards the ten array ports P13, P14, ..., P22 is reported in Figure 13; the effects of the dummy ports are particularly evident in the left side of the lens. The phase error is quite satisfactory, from the data reported in Figure 14; the phase error is always below 1.5 degrees as in the previous experiment.

In the last experiment, a Rotman lens at the K band (22–26 GHz) has been considered. The considered lens structure is characterised by six input beam ports, with a steering angle of 35 degrees, four dummy ports, and twelve output array ports. The considered central frequency is $f_c = 24.0$ GHz, and the port impedance is 50 Ω. The other lens geometrical characteristics are focal length $f_1 = 5.0\lambda$, focal angle $\alpha = 35$ degrees, focal ratio $\widetilde{\beta} = f_2/f_1 = 0.9$, and expansion factor $\gamma = 1$. The length of the tapered line $L_t = 1\lambda$, and the length of microstrip lines connected with the beam and array ports $L_m = 0.5\lambda$.

The width of the beam, array, and dummy tapered sections is $w_{tb} = 26$ mm, $w_{ta} = 8.5$ mm, and $w_{td} = 25.32$ mm, respectively. The length of the tapered lines and of the 50 Ω transmission lines which connect the ports is 1.5λ and 0.5λ, respectively. The port positions and the geometry of the K-band Rotman lens, obtained after the IA procedure and the refinement algorithm, are reported in Figures 15

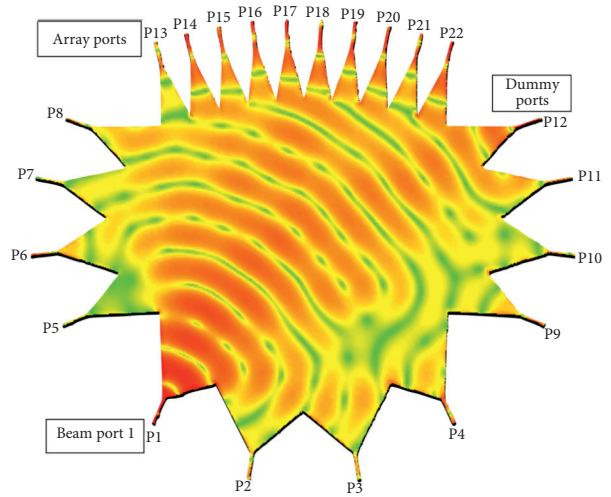

Figure 7: S-band Rotman lens: current distribution with beam port −2 feeded in the range between 2.0 GHz and 3.0 GHz.

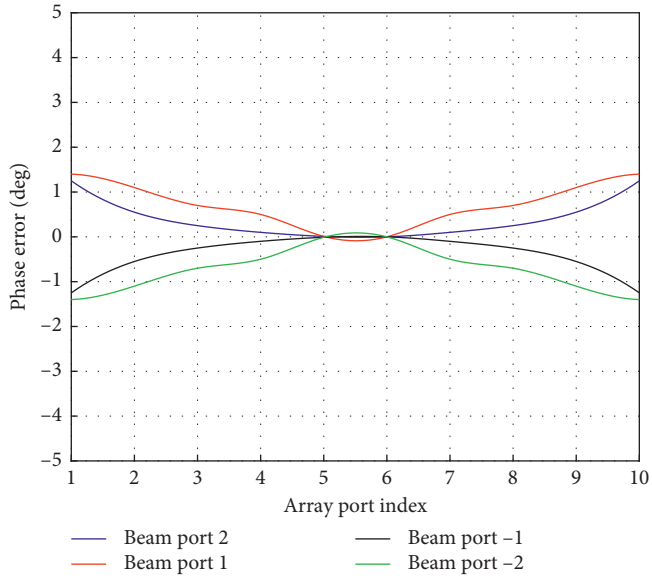

Figure 8: S-band Rotman lens: phase errors at the array ports.

and 16, respectively. The return loss at the six input beam ports P1–P6 is quite satisfactory and always within the limits, $-13\,\text{dB} > S_{11} > -24\,\text{dB}$, predicted by the IA procedure, as reported in Figure 17. Also, the isolation between the input beam ports is quite good; in particular, the nearest ports P1 and P2 show isolation below −20 dB, while the isolation of about −28 dB is measured between ports P1 and P6, as reported in Figures 18(a) and 18(b). The current distribution between each input beam port and the array ports is reported in Figures 19(a)–19(f). As it can be noticed from the data reported in Figure 19, the focusing effect of the Rotman lens is quite evident. Concerning the phase error at the array ports, the maximum measured phase error at the ports placed far away from the lens centre was below 2.5 degrees, while the error at the mechanical boresight of the lens was below 1.5 degrees. The phase errors are higher concerning the other lens structures considered in the previous experiments, as expected since the wavelength is lower.

3.2. Experimental Assessment. In this section, an experimental X-band Rotman lens prototype has been designed, fabricated, and assessed. The considered Rotman lens parameters are the following: six input beam ports, scan angle of ± 30 degrees, and centre frequency of 10 GHz with a 4 GHz bandwidth to cover the whole X-band range. The high bandwidth provided by the Rotman lens feeding network is strongly limited to 500 MHz, by the radiators (rectangular patch antennas equipped with a quarter wavelength-matching transformer). Sixteen array ports are connected to sixteen antennas with an interelement spacing of 0.4λ.

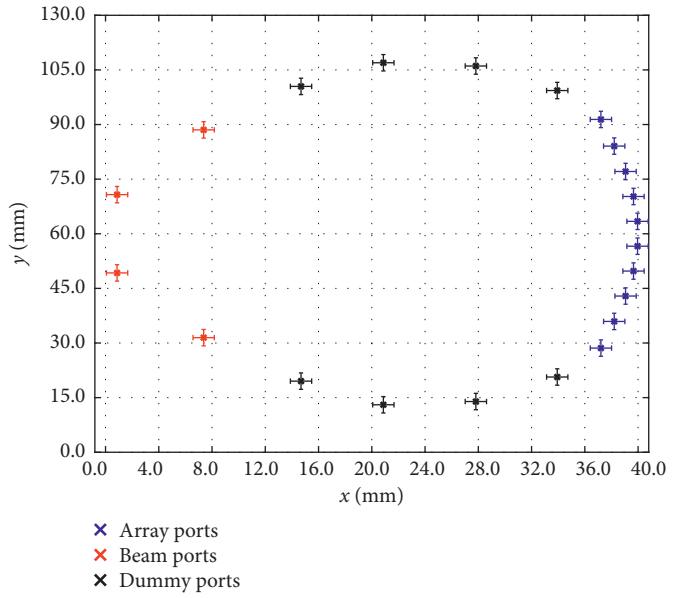

Figure 9: C-band Rotman lens: port positions and position tolerances after IA refinement.

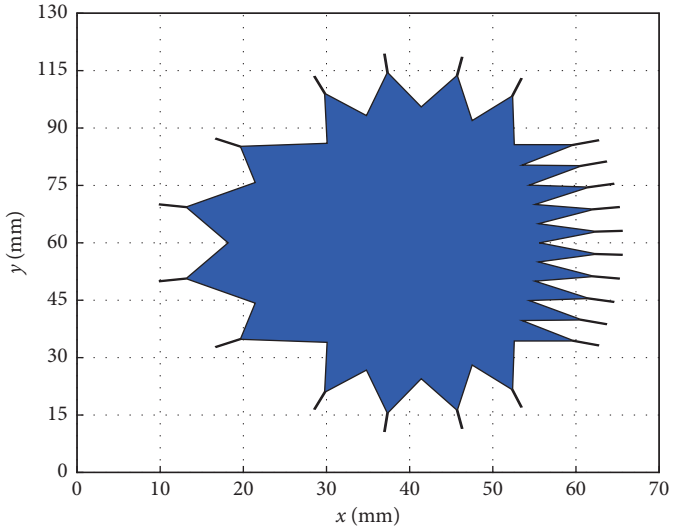

Figure 10: C-band Rotman lens geometry.

Summarizing the feeding network is characterised by $N_a = 16$ array ports, $N_b = 6$ beam ports, and $N_d = 4$ dummy ports. Other lens parameters are as follows: a focal length $f_1 = 6$, a focal angle $\alpha = 35$ degrees, a focal ratio $\beta = f_2/f_1 = 0.9$, an expansion factor $\gamma = 1$, and a port impedance = 50 Ω. The lens is realised considering a ceramic substrate Arlon 25N of 0.5 mm thickness with a dielectric permittivity $\varepsilon_r = 3.28$ and $\tan(\delta) = 10^{-3}$. A circular curvature lens on the beam and array ports has been considered, and four dummy ports are aimed at absorbing energy reflections at the top and bottom sides of the lens structure. All ports are connected with tapered transmission lines which are aligned towards the lens centre, and the tapered lines are aimed at guaranteeing a good impedance matching, good beams, and a phase error reduction. To apply formulas (1)–(4) for the geometrical estimation of geometrical lens parameters with the IA, the following interval tolerances have been considered: $\tilde{\varepsilon}_r = \{3.23; 3.33\}$, $\tilde{t} = \{0.43; 0.57\}$ (mm), $\tilde{t}_m = \{8; 12\}$ (μm), and $L = \{L - 0.05; L + 0.05\}$ (mm), with L being a geometrical parameter indicating a given length. After the application of design formulas and the Skelboe–Moore refinement algorithm [32], beam, array, and dummy port positions are estimated. Figure 20 shows the positions of the ports with the intervals of confidences provided by the upper and lower limits. The exact port coordinates are reported in Tables 1–3 which report the positions of the array, beam, and dummy ports, respectively. The width of the beam, array, and dummy tapered sections is $w_{tb} = 26$ mm, $w_{ta} = 8.5$ mm, and $w_{td} = 25.32$ mm. The length of the tapered lines and of the 50 Ω transmission lines which connect the ports is 1.5λ and 0.5λ, respectively. The geometry of the obtained Rotman lens is shown in Figure 21.

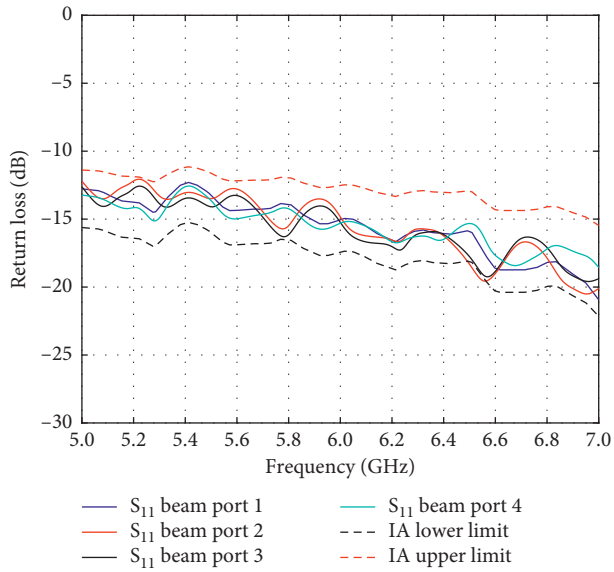

Figure 11: C-band Rotman lens: return loss at the beam ports.

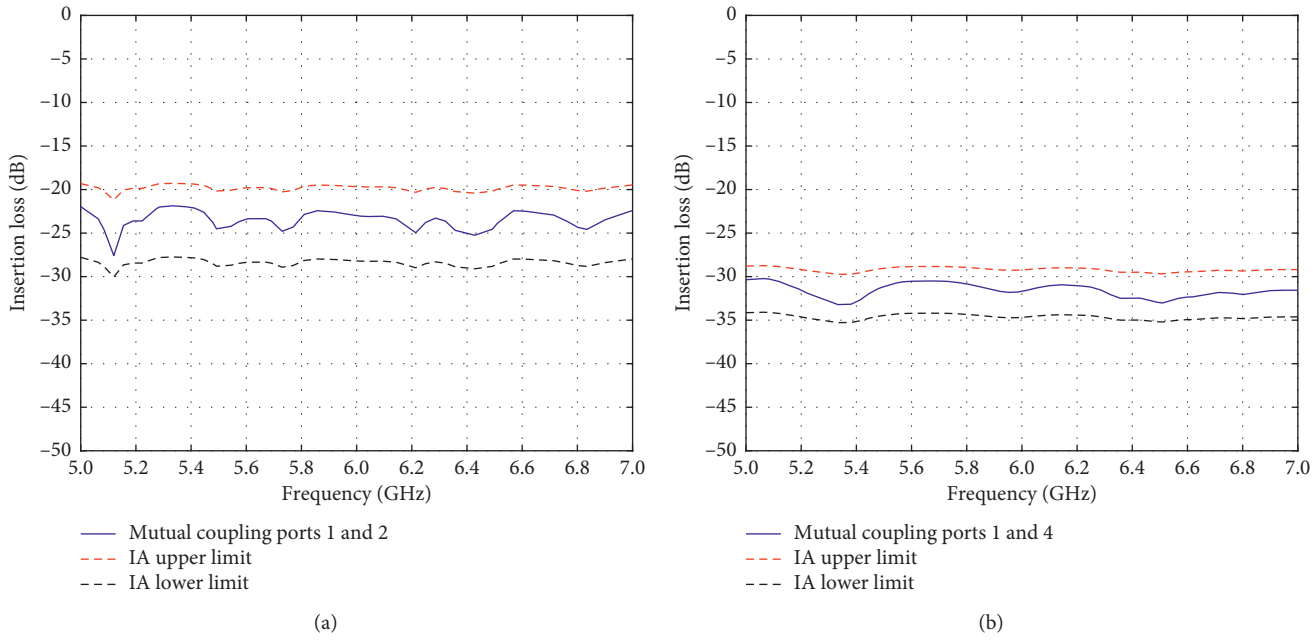

Figure 12: C-band Rotman lens: coupling factor vs. frequency (a) between ports P1 and P2 and (b) between ports P1 and P4.

The phase errors at the array ports have been estimated by considering relation (6), and the results are shown in Figure 22. As expected, the higher phase errors can be found where the ports are placed far away from the lens boresight, and it can be noticed from the data in Figure 22 that the maximum phase error is about ± 2 degrees, while the amplitude errors at the outer ports are about 1.5 dB. The correspondent computed lens array factor for all the beam ports is reported in Figure 23.

3.3. X-Band Prototype Description. After the IA design procedure and the preliminary numerical estimation of the lens characteristics, an antenna array prototype, with a Rotman lens as a feeding network, has been fabricated and assessed. In particular, sixteen rectangular patch antennas equipped with a quarter wavelength transformer have been connected to the $N_a = 16$ array ports with sixteen microstrip lines; each length has been estimated by solving equation (2). The lens geometrical parameters are retrieved from Tables 1–3.

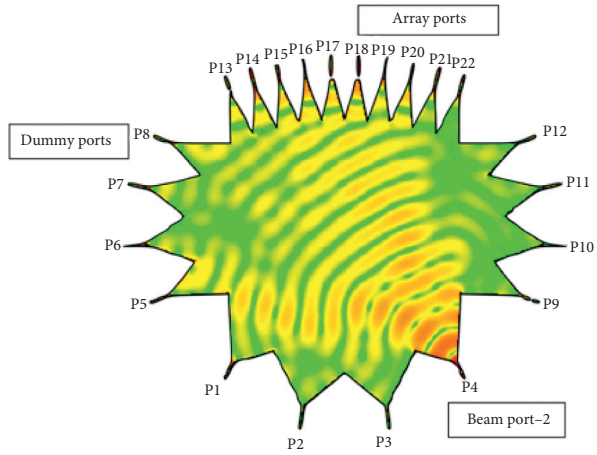

Figure 13: C-band Rotman lens: current distribution with beam port −2 feeded at $f_c = 5.8$ GHz.

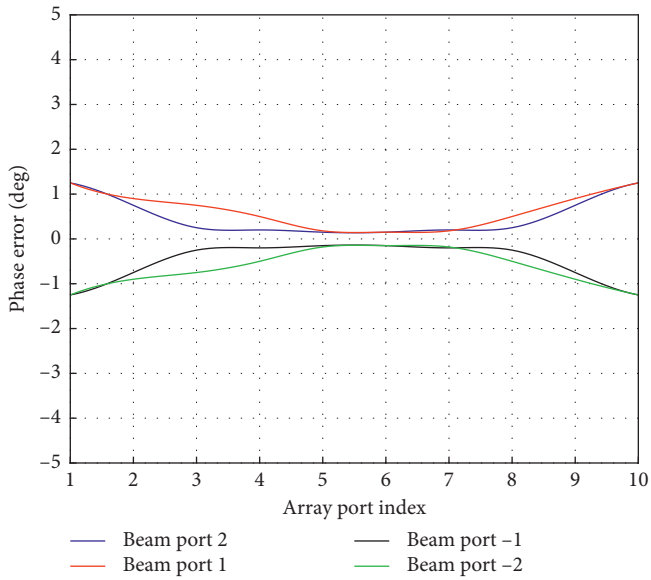

Figure 14: C-band Rotman lens: phase errors at the array ports.

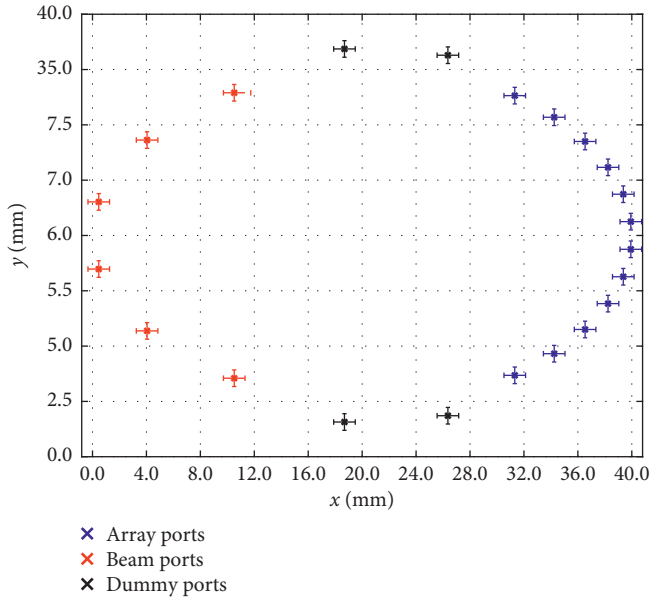

Figure 15: K-band Rotman lens: port positions and position tolerances after IA refinement.

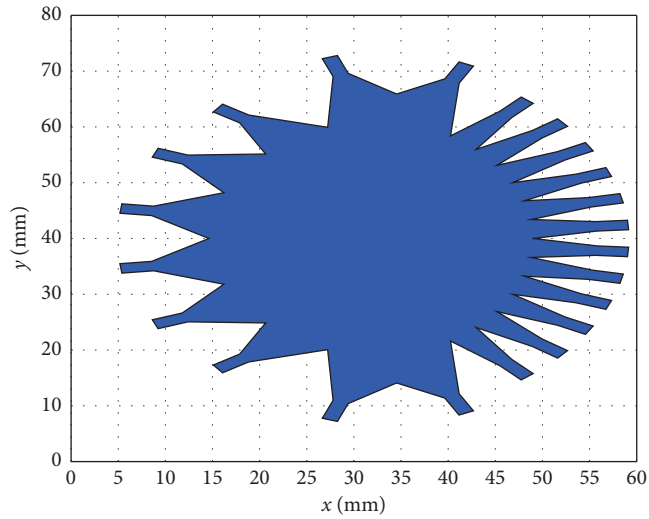

Figure 16: K-band Rotman lens geometry.

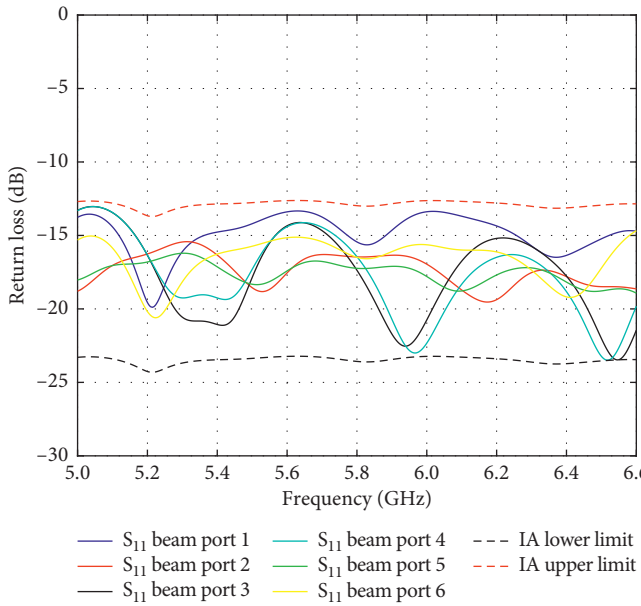

Figure 17: K-band Rotman lens: return loss at the beam ports.

The prototype has been obtained with a CNC milling machine with a mechanical resolution of 0.05 mm. The prototype is shown in Figure 24: it has been equipped with ten subminiature type A (SMA) coaxial connectors to measure the prototype scattering parameters. An experimental setup has been arranged in an anechoic chamber. The first set of measurements concerns the estimation of the return loss at the beam ports. For the sake of comparisons, the measurements have been compared with the simulation obtained with commercial software, namely, ADS 2019. In particular, the insertion loss measures are reported in Figure 25, which also states the synthetic results obtained with ADS and considering the upper and lower limits of the geometrical lens parameters provided by the IA approach. It can be noticed from the data in Figure 25 that the measured insertion loss is quite satisfying: below −12 dB for all the considered frequency range. The second set of measures is related to the estimation of the isolation between the beam ports. In particular, the insertion loss parameter has been estimated for each couple of ports. In particular, Figures 26(a)and 26(b) report the measured insertion loss between two adjacent ports (ports P1 and P2) and between two distant ports (ports P1 and P6). It can be noticed from the data in Figure 26 that the isolation between the beam ports is very good: about −22 dB and −32 dB for the adjacent and distant ports, respectively.

Also, the measured data have been compared with the simulated ones and by considering the upper and lower IA limits. The predicted and measured values are very similar. Figure 27 shows the measured array pattern rosettes at 10 GHz for beams 1–6.

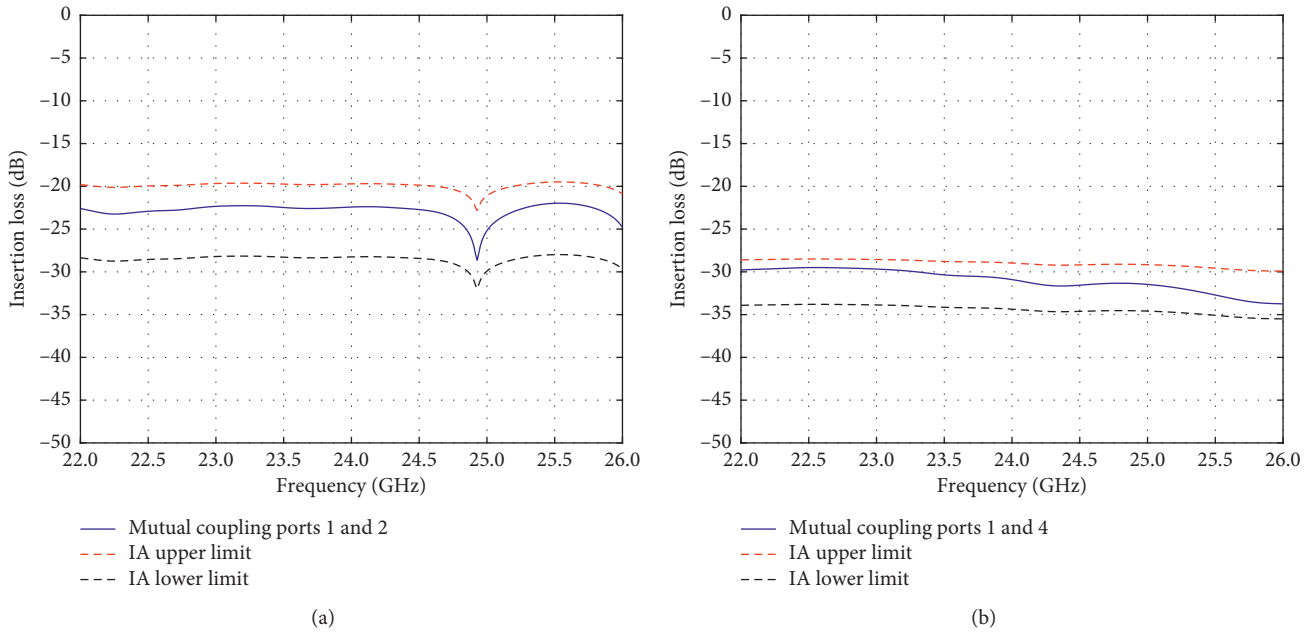

FIGURE 18: K-band Rotman lens: coupling factor vs. frequency (a) between ports P1 and P2 and (b) between ports P1 and P6.

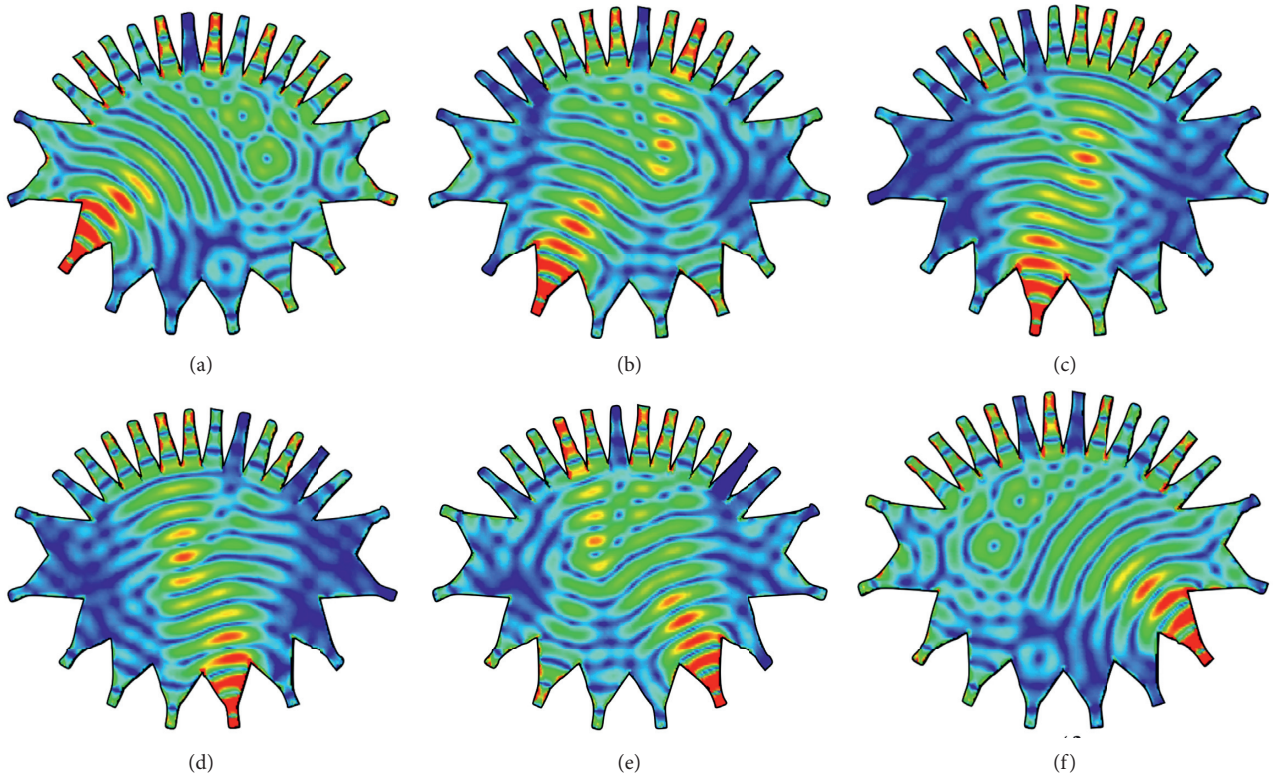

FIGURE 19: K-band Rotman lens: current distribution in (a) port 3, (b) ports 2, (c) port 1, (d) port −1, (e) port −2, and (f) port −3 at f_c = 24.0 GHz.

Moreover, it can be noticed that the main beam is correctly steered towards the angular direction of the ports. In particular, Table 4 reports the required and the measured direction of the main beam. As it can be noticed, the higher measured error is +3 degrees. The shape of the main beam is quite regular, and the secondary side lobe (SSL) level is satisfactory and comparable with the simulated results obtained with ADS.

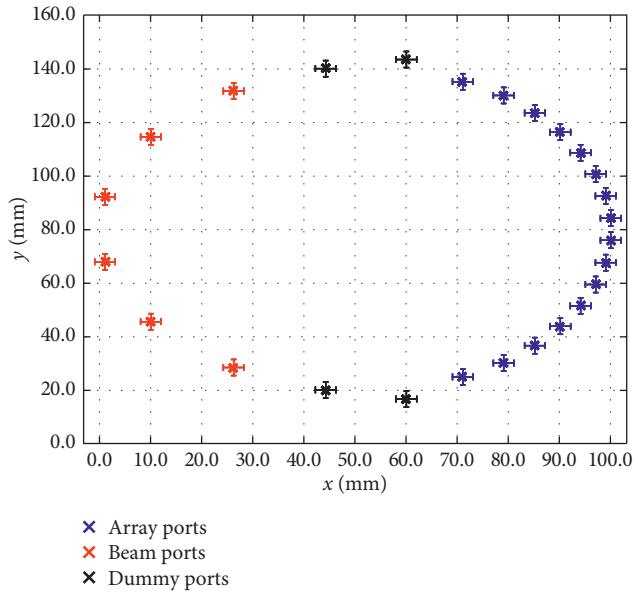

Figure 20: X-band Rotman lens prototype: port positions and position tolerances after IA refinement.

Table 1: Array port positions (mm).

	P1	P2	P3	P4	P5	P6	P7	P8	P9	P10	P11	P12	P13	P14	P15	P16
x_n^{ap}	130.11	138.21	145.05	150.22	153.11	155.32	157.92	158.51	159.01	158.02	156.32	153.65	148.06	143.41	137.42	130.02
y_n^{ap}	55.10	58.52	66.01	73.42	81.33	89.00	97.54	102.11	115.43	124.14	131.02	138.11	142.71	155.02	162.31	164.21

Table 2: Beam port positions (mm).

	P1	P2	P3	P4	P5	P6
x_n^{bp}	85.13	70.15	59.12	59.11	70.34	85.31
y_n^{bp}	55.25	76.11	97.24	122.23	145.03	160.14

Table 3: Dummy port positions (mm).

	P1	P2	P3	P4
x_n^{dp}	102.51	117.11	102.52.12	117.43
y_n^{dp}	44.51	47.12	174.41	177.31

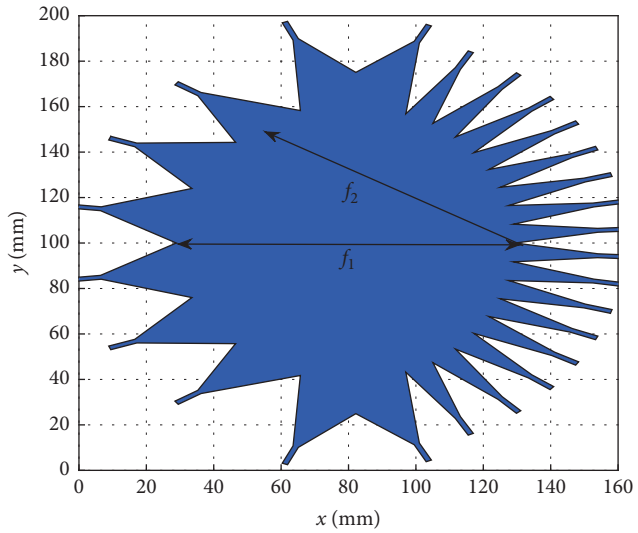

Figure 21: Geometry of the X-band Rotman lens.

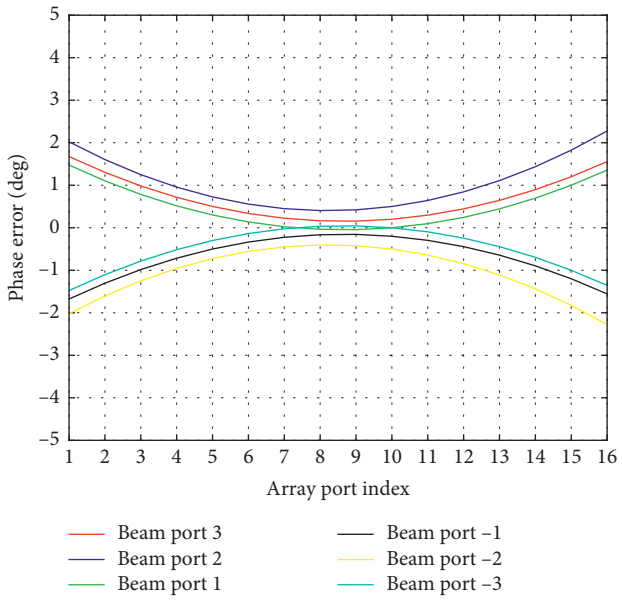

Figure 22: Array port phase errors.

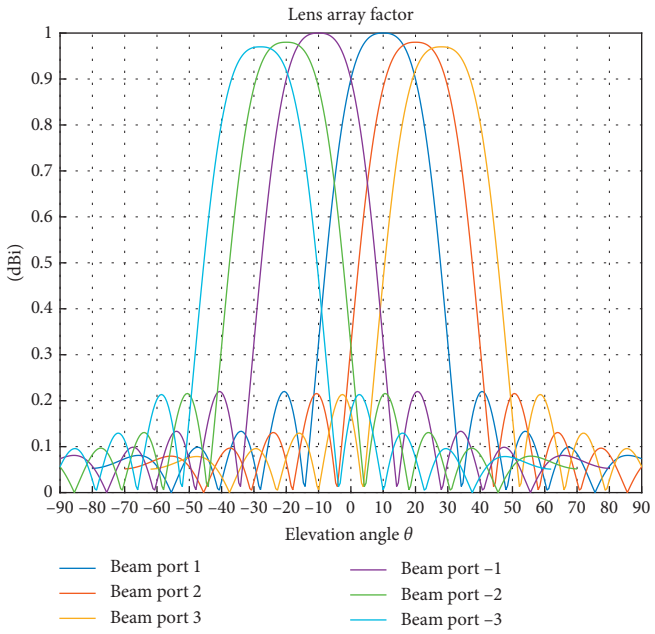

Figure 23: Rotman lens array factor rosette.

Figures 28 and 29 report the comparisons of predicted and measured beam patterns related to beam ports p_{-1} and p_3, respectively. The numerical values have been obtained considering the upper and lower geometrical parameters provided by the IA rules and the refinement algorithm. It can be noticed that the measured main beam is precisely located between the beams obtained by considering the upper and lower IA limits, demonstrating the effectiveness of the proposed method.

4. Conclusion

An innovative approach based on interval analysis and the arithmetic of intervals has been proposed for the design of Rotman lens feeding networks when manufacturing errors are present. The problem of the Rotman lens feeding network design has been first recast into the IA-based framework by introducing the interval numbers aimed at describing the tolerances on the lens parameters and the arising lens illumination function. The proposed method is able to (i) manage the uncertainties and the tolerance errors due to the materials and fabrication process and (ii) define exact and analytical bounds of the lens parameters and the corresponding illumination function by using the rules of interval arithmetic. The obtained results have shown the potential of the proposed strategy; in particular, a prototype working in the X band has been designed, fabricated, and experimentally assessed. Further advances will consider the extension of the proposed method to the analysis of waveguide-based Rotman lenses.

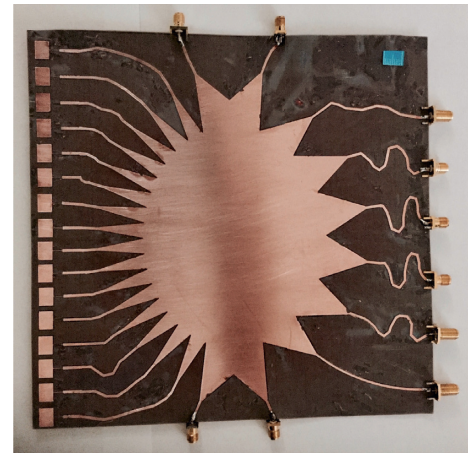

Figure 24: Photo of the Rotman lens prototype equipped with SMA coaxial connectors.

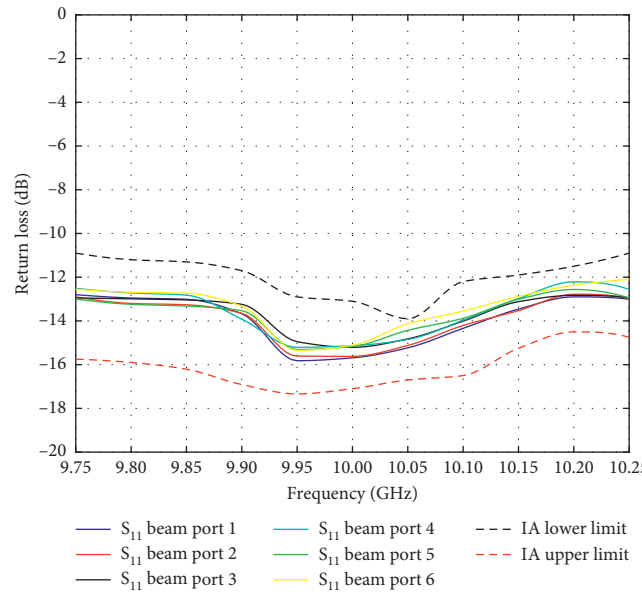

Figure 25: Insertion loss measured at the beam ports.

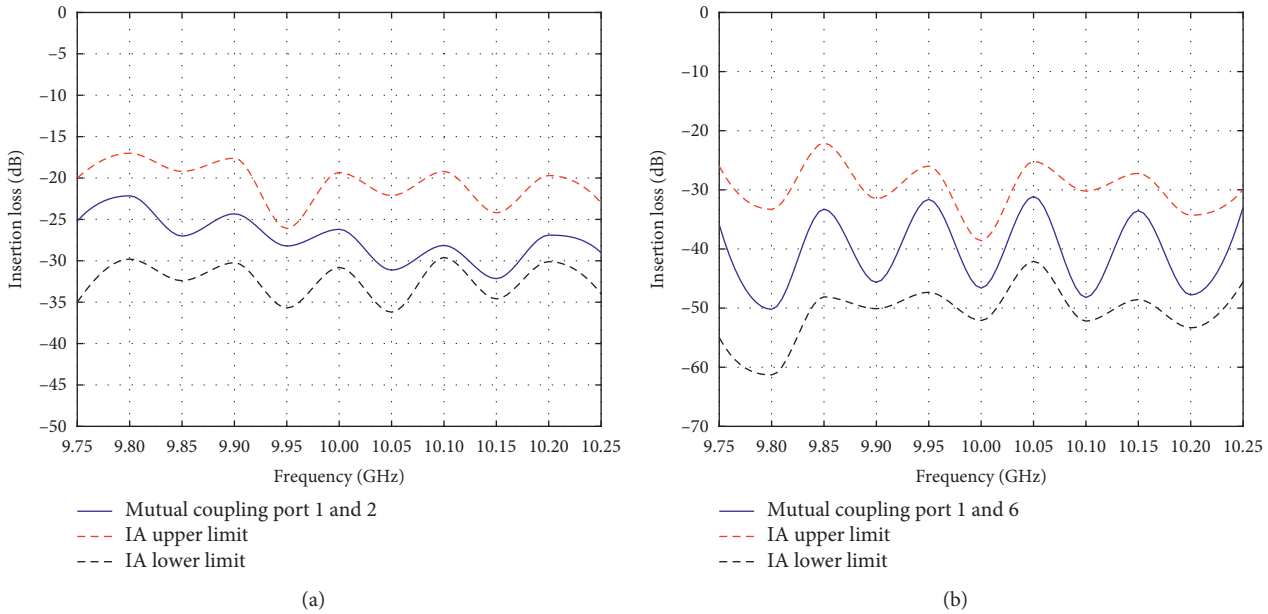

Figure 26: Measurement of the coupling factor between (a) ports P1 and P2 and (b) ports P1 and P6.

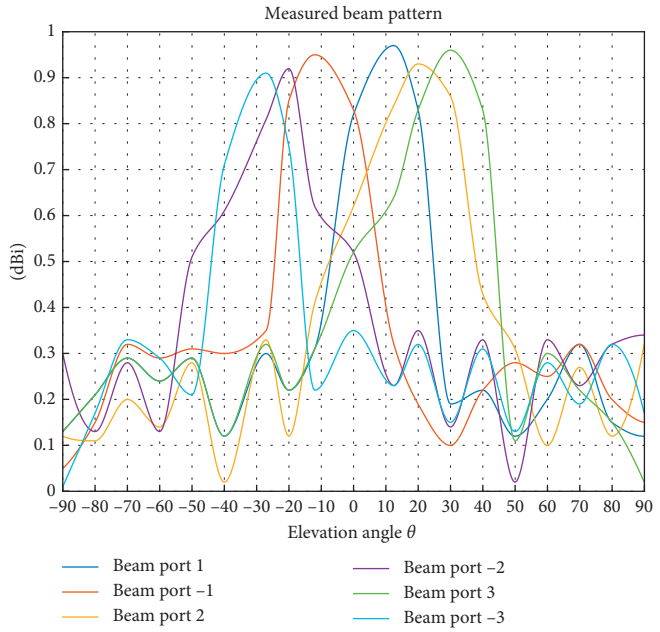

Figure 27: Measured beam patterns at the six beam ports.

Table 4: Beam steering directions (degrees).

	θ_{req}	θ_{mean}	θ_{err}
$p_{\bar{1}}^{bp}$	−10.0	−12.0	2.0
$p_{\bar{2}}^{bp}$	−20.0	−21.0	1.0
$p_{\bar{3}}^{bp}$	−30	−27.0	3.0
p_1^{bp}	10.0	12.5	2.5
p_2^{bp}	20.0	21.5	1.5
p_3^{bp}	30.0	31.5	1.5

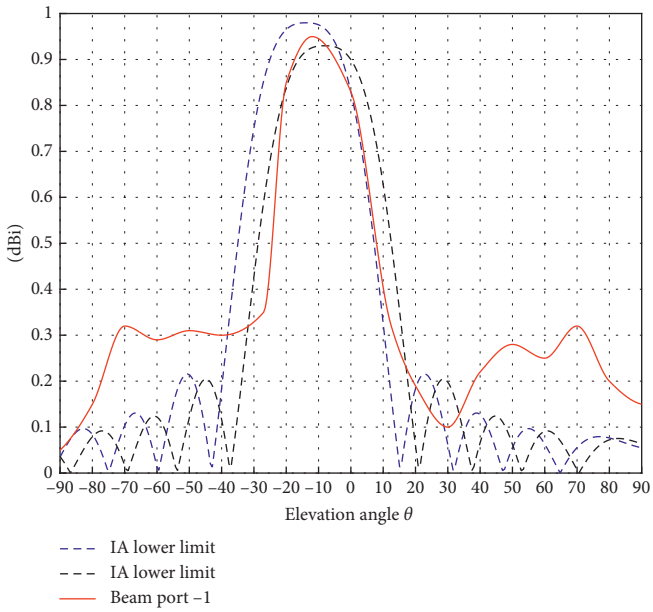

Figure 28: Measured vs. simulated beam pattern considering the lower and upper IA limits. Beam port −1, beam steering at −10 degrees.

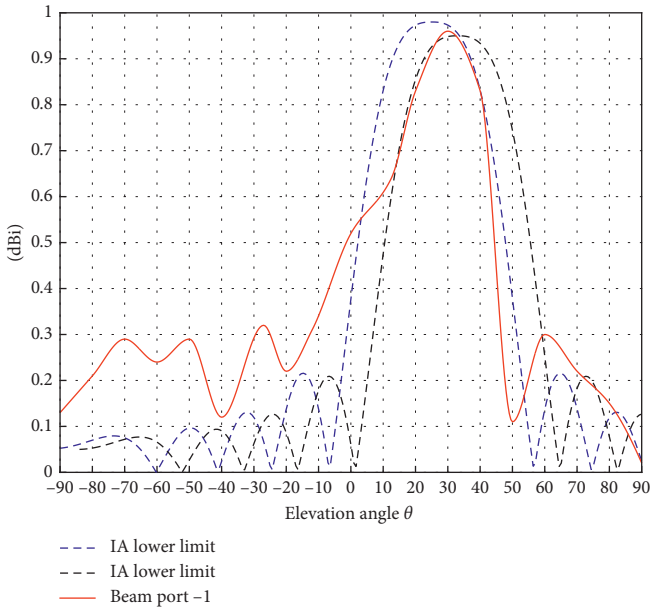

Figure 29: Measured vs. simulated beam pattern considering the lower and upper IA limits. Beam port 3, beam steering at +30 degrees.

Appendix

Microstrip Rotman Lens Design

In order to design and calculate the parameters of a microstrip lens, a mathematical model is formulated, as shown in Figure 30. However, most of it has been explained in Section 2. In the figure, the beam ports and array ports are

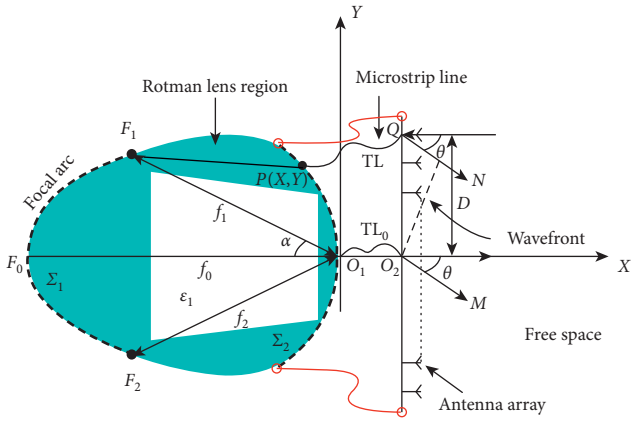

Figure 30: Microstrip Rotman lens parameters.

denoted as Σ_1 and Σ_2, respectively, and F_0, F_1, and F_2 are focal points with coordinates $(-f_1 \cos\alpha, f_1 \sin\alpha)$, $(-f_2 \cos\alpha, -f_2 \sin\alpha)$, and $(-f_0, 0)$. The wave path length of the wave passing $\overline{O_1 F_1 O_1 O_2 M}$ should be equal to the wave path length of $\overline{F_1 PQN}$ and $\overline{F_2 PQN}$, which can be calculated by the following equation. An angle of the main beam direction θ corresponds to the focal point f_1. The antenna array is parallel to the Y-axis, and the coordinate of the antenna at the focal point f_1 is $(0, D)$. In the following, the key part of the microstrip Rotman lens arithmetic is summarized.

$$\sqrt{\varepsilon_r}\left(\overrightarrow{F_1P}\right) + \sqrt{\varepsilon_{\text{eff}}}\,W + D\sin\theta = \sqrt{\varepsilon_r} f_1 + \sqrt{\varepsilon_{\text{eff}}}\,W_0, \tag{A.1}$$

$$\sqrt{\varepsilon_r}\left(\overrightarrow{F_2P}\right) + \sqrt{\varepsilon_{\text{eff}}}\,W - D\sin\theta = \sqrt{\varepsilon_r} f_2 + \sqrt{\varepsilon_{\text{eff}}}\,W_0, \tag{A.2}$$

$$\sqrt{\varepsilon_r}\left(\overrightarrow{F_0P}\right) + \sqrt{\varepsilon_{\text{eff}}}\,W = \sqrt{\varepsilon_r} f_0 + \sqrt{\varepsilon_{\text{eff}}}\,W_0, \tag{A.3}$$

where ε_{eff} and ε_r are the dielectric constant of the microstrip line and relative dielectric constant of the substrate, respectively.

$$\left(\overrightarrow{F_1P}\right)^2 = f_1^2 + X^2 + Y^2 + 2FX\cos\alpha - 2FY\sin\alpha, \tag{A.4}$$

$$\left(\overrightarrow{F_2P}\right)^2 = f_2^2 + X^2 + Y^2 + 2FX\cos\alpha + 2FY\sin\alpha, \tag{A.5}$$

$$\left(\overrightarrow{F_0P}\right)^2 = (X + f_0)^2 + Y^2. \tag{A.6}$$

Here, $f_1 = f_2$. Assuming $f = f_1 = f_2$ and dividing $\sqrt{\varepsilon_r} f$ in equations (A.1)–(A.3),

$$\frac{\left(\overrightarrow{F_1P}\right)}{f} = 1 - \sqrt{\frac{\varepsilon_{\text{eff}}}{\varepsilon_r}}\,\frac{W - W_0}{f} - \frac{1}{\sqrt{\varepsilon_r}}\,\frac{D}{f}\sin\theta, \tag{A.7}$$

$$\frac{\left(\overrightarrow{F_2P}\right)}{f} = 1 - \sqrt{\frac{\varepsilon_{\text{eff}}}{\varepsilon_r}}\,\frac{W - W_0}{f} + \frac{1}{\sqrt{\varepsilon_r}}\,\frac{D}{f}\sin\theta, \tag{A.8}$$

$$\frac{\left(\overrightarrow{F_0P}\right)}{f} = \frac{f_0}{f} - \sqrt{\frac{\varepsilon_{\text{eff}}}{\varepsilon_r}}\,\frac{W - W_0}{f}. \tag{A.9}$$

By assuming $\widetilde{w} = \sqrt{\varepsilon_{\text{eff}}/\varepsilon_r}\,(W - W_0)/f$, $\eta = 1/\sqrt{\varepsilon_r}D/f$, $g = f_0/f$, $a_1 = \cos\theta$, and $b_1 = \cos\theta$ and then rewriting equations (A.7)–(A.9),

$$\frac{\left(\overrightarrow{F_1P}\right)}{f} = 1 - \widetilde{w} - \eta b_1, \tag{A.10}$$

$$\frac{\left(\overrightarrow{F_2P}\right)}{f} = 1 - \widetilde{w} + \eta b_1, \tag{A.11}$$

$$\frac{\left(\overrightarrow{F_0P}\right)}{f} = g - \widetilde{w}. \tag{A.12}$$

Letting $a_0 = \cos\alpha$, $b_0 = \sin\alpha$, $x = X/f$, and $y = Y/f$ and by rewriting equations (A.4)–(A.6),

$$\frac{\left(\overrightarrow{F_1P}\right)^2}{f^2} = 1 + x^2 + y^2 + 2a_0x - 2b_0y, \tag{A.13}$$

$$\frac{\left(\overrightarrow{F_2P}\right)^2}{f^2} = 1 + x^2 + y^2 + 2a_0x + 2b_0y, \tag{A.14}$$

$$\frac{\left(\overrightarrow{F_0P}\right)^2}{f^2} = (x + g)^2 + y^2. \tag{A.15}$$

By substituting equation (A.10) into equation (A.13),

$$\begin{aligned}\left(1 - \widetilde{w} - \eta b_1\right)^2 &= 1 + \widetilde{w}^2 + b_1^2\eta^2 - 2b_1\eta + 2b_1\widetilde{w}\eta - 2\widetilde{w} \\ &= 1 + x^2 + y^2 + 2a_0x - 2b_0y.\end{aligned} \tag{A.16}$$

If η is replaced by $-\eta$ and y by $-y$, then

$$\begin{aligned}1 + \widetilde{w}^2 + b_1^2\eta^2 + 2b_1\eta - 2b_1\widetilde{w}\eta - 2\widetilde{w} &= 1 + x^2 + y^2 \\ &+ 2a_0x + 2b_0y.\end{aligned} \tag{A.17}$$

From equations (A.16) and (A.17), we can derive

$$y = \frac{b_1}{b_0}\eta(1 - \widetilde{w}), \tag{A.18}$$

$$x^2 + y^2 + 2a_0x = \widetilde{w}^2 + b_1^2\eta^2 - 2\widetilde{w}. \tag{A.19}$$

By substituting equation (A.12) into equation (A.15),

$$\begin{aligned}(g - \widetilde{w})^2 &= (x + g)^2 + y^2, \\ \text{or } x^2 + y^2 + 2gx &= \widetilde{w}^2 - 2g\widetilde{w}.\end{aligned} \tag{A.20}$$

From equations (A.18)–(A.20),

$$\widetilde{a}\widetilde{w}^2 + \widetilde{b}\widetilde{w} + \widetilde{c} = 0, \tag{A.21}$$

$$\widetilde{w} = \frac{-b \pm \sqrt{b^2 - 4ac}}{2a}. \tag{A.22}$$

By solving algebraic equation (A.21) for given parameters θ (the maximum scanning angle), α, and g and using $\widetilde{w}$ as a function of η,

$$\begin{aligned}\widetilde{a} &= 1 - \left(\frac{b_1}{b_0}\eta\right)^2 - \left(\frac{g - 1}{g - a_0}\right)^2, \\ \widetilde{b} &= 2g\left(\frac{a_0 - 1}{g - a_0}\right) + \left(\frac{2}{b_0^2} - \frac{g - 1}{(g - a_0)^2}\right)b_1^2\eta^2, \\ \widetilde{c} &= \frac{gb_1^2\eta^2}{g - a_0} + \frac{b_1^4\eta^4}{4(g - a_0)^2} - \left(\frac{b_1}{b_0}\eta\right)^2.\end{aligned} \tag{A.23}$$

Data Availability

All data come from simulations and measurement, and the geometrical parameters of the developed prototype can be easily reproduced with a CAD tool.

Conflicts of Interest

The authors declare that there are no conflicts of interest regarding the publication of this paper.

Acknowledgments

The authors would like to thank Dr. E. Bortolotti for the revision of the manuscript.

References

[1] R. L. Haupt, "Phase-only adaptive nulling with a genetic algorithm," *IEEE Transactions on Antennas and Propagation*, vol. 45, no. 6, pp. 1009–1015, 1997.

[2] D. S. Weile and E. Michielssen, "The control of adaptive antenna arrays with genetic algorithms using dominance and diploidy," *IEEE Transactions on Antennas and Propagation*, vol. 49, no. 10, pp. 1424–1433, 2001.

[3] S. Caorsi, M. Donelli, A. Lommi, and A. Massa, "A new GA-based strategy for adaptive antenna array control," in *Proceedings of the JINA2002*, pp. 447–450, Nice, France, November 2002.

[4] C. Sacchi, F. De Natale, M. Donelli, A. Lommi, and A. Massa, "Adaptive antenna array control in presence of interfering signals with stochastic arrival assessment of a GA-based procedure," *IEEE Transactions on Wireless Communications*, vol. 3, no. 4, pp. 1031–1036, 2004.

[5] A. A. Salih, Z. N. Chen, and K. Mouthaan, "Characteristic mode analysis and metasurface based suppression of higher-order modes of a closely spaced phased array," *IEEE Transactions on Antennas and Propagation*, vol. 65, no. 3, pp. 1141–1150, 2017.

[6] D. Gesbert, M. Shafi, D. Shiu, P. J. Smith, and A. Naquib, "From theory to practice: an overview of MIMO space-time coded wireless systems," *IEEE Journal on Selected Areas in Communications*, vol. 21, no. 3, pp. 281–302, 2003.

[7] K. Gyoda and T. Ohira, "Design of electronically steerable passive array radiator (ESPAR) antennas," in *Proceedings of the Antennas and Propagation Society International Symposium*, vol. 2, pp. 922–925, Atlanta, GA, USA, July 2000.

[8] M. D. Migliore, D. Pinchera, and F. Schettino, "A simple and robust adaptive parasitic antenna," *IEEE Transactions on Antennas and Propagation*, vol. 53, no. 10, pp. 3262–3272, 2005.

[9] P. de Maagt, R. Gonzalo, Y. C. Vardaxoglou, and J.-M. Baracco, "Electromagnetic bandgap antennas and components for microwave and (sub) millimeter wave applications," *IEEE Transactions on Antennas and Propagation*, vol. 51, no. 10, pp. 2667–2677, 2003.

[10] R. Azaro, M. Donelli, L. Fimognari, and A. Massa, "A planar electronically reconfigurable Wi-Fi band antenna based on parasitic microstrip structures," *IEEE Antennas and Wireless Propagation Letters*, vol. 6, pp. 623–626, 2007.

[11] R. Azaro, M. Donelli, M. Benedetti et al., "Design and optimization of reconfigurable parasitic antennas by means of PSO-based techniques," in *Proceedings of the International Review of Progress in Applied Computational Electromagnetics, 24th ACES*, Niagara Falls, Canada, March 2008.

[12] P. Rocca, M. Donelli, A. Massa, F. Viani, and G. Oliveri, "Reconfigurable sum-difference pattern by means of parasitic elements for forward-looking monopulse radar," *IET Radar, Sonar & Navigation*, vol. 7, no. 7, pp. 747–754, 2013.

[13] W. Rotman and R. F. Turner, "Wide-angle microwave lens for line Source applications," Report AFCRL-62-18 AF, Cambridge Research Laboratories, Bedford, MA, USA, 1962.

[14] W. Rotman and R. F. Turner, "Wide-angle microwave lens for line source applications," *IEEE Transactions on Antennas and Propagation*, vol. 11, no. 6, pp. 623–632, 1963.

[15] M. J. Maybell, "Printed rotman lens-fed array having wide bandwidth, low sidelobes, constant beamwidth, and synthesised radiation pattern," in *Proceedings of the 1983 Antennas and Propagation Society International Symposium*, pp. 373–376, Houston, TX, USA, May 1983.

[16] T. Katagi, S. Mano, and S. Sato, "An improved design method of Rotman lens antennas," *IEEE Transactions on Antennas and Propagation*, vol. 32, no. 2, pp. 524–527, 1984.

[17] K. K. Chan and S. K. Rao, "Design of a Rotman lens feed network to generate a hexagonal lattice of multiple beams," *IEEE Transactions on Antennas and Propagation*, vol. 50, no. 8, pp. 1099–1108, 2002.

[18] L. Hall, D. Abbott, and H. Hansen, "Rotman lens for mm-wavelengths," in *Proceedings of SPIE—The International Society for Optical Engineering (SPIE2002)*, pp. 215–221, San Jose, CA, USA, January 2002.

[19] P. S. Simon, "Analysis and synthesis of rotman lenses," in *Proceedings of the 22nd AIAA International Communications Satellite Systems Conference & Exhibit 2004 (ICSSC)*, pp. 1–11, Monterey, CA, USA, May 2004.

[20] D. H. Archer and M. J. Maybell, "Rotman lens development history at Raytheon electronic warfare systems 1967–1995," in *Proceedings of the 2005 IEEE Antennas and Propagation Society International Symposium*, pp. 31–34, Washington, DC, USA, July 2005.

[21] C. Penney, "Rotman lens design and simulation in software," *IEEE Microwave Magazine*, vol. 9, no. 6, pp. 138–149, 2008.

[22] R. P. S. Kushwah and P. K. Singhal, "Modified design of bootlace lens for multiple beamforming," *Journal of Electrical and Electronics Engineering Research*, vol. 2, pp. 14–24, 2010.

[23] Y. Zhang, S. Christie, V. Fusco, R. Cahill, G. Goussetis, and D. Linton, "Reconfigurable beam forming using phase-aligned Rotman lens," *IET Microwaves, Antennas & Propagation*, vol. 6, no. 3, pp. 326–330, 2012.

[24] J. Hasch, E. Topak, R. Schnabel, T. Zwick, R. Weigel, and C. Wald- schmidt, "Millimeter-wave technology for automotive radar sensors in the 77 GHz frequency band," *IEEE Trans. Microwave Theory and Techniques*, vol. 60, no. 3, 2012.

[25] X. Zou, C.-M. Tong, J.-S. Bao, and W.-J. Pang, "SIW-fed yagi antenna and its application on monopulse antenna," *IEEE Antennas and Wireless Propagation Letters*, vol. 13, pp. 1035–1038, 2014.

[26] A. Darvazehban, O. Manoochehri, M. A. Salari, P. Dehkhoda, and A. Tavakoli, "Ultra-wideband scanning antenna array with Rotman lens," *IEEE Trans. Microwave Theory and Techniques*, vol. 65, no. 9, pp. 3435–3442, 2017.

[27] H.-T. Chou and C.-Y. Chang, "Application of rotman lens beamformer for relatively flexible multibeam coverage from electrically large-phased arrays of antennas," *IEEE Transactions on Antennas and Propagation*, vol. 67, no. 5, pp. 3058–3066, 2019.

[28] N. Kou, S. Yu, Z. Ding, and Z. Zhang, "One-dimensional beam scanning transmitarray lens antenna fed by microstrip linear array," *IEEE Access*, vol. 7, pp. 90731–90740, 2019.

[29] Y. Liu, H. Yang, Z. Jin, and J. Zhu, "Circumferentially conformal slot array antenna and its Ka-band multibeam applications," *IET Microwaves, Antennas & Propagation*, vol. 12, no. 15, pp. 2307–2312, 2018.

[30] E. H. Mujammami, I. Afifi, and A. B. Sebak, "Optimum wideband high gain analog beamforming network for 5G applications," *IEEE Access*, vol. 7, pp. 52226–52237, 2019.

[31] X. Wang, A. Akbarzadeh, L. Zou, and C. Caloz, "Flexible-resolution, arbitrary-input, and tunable rotman lens spectrum decomposer," *IEEE Transactions on Antennas and Propagation*, vol. 66, no. 8, pp. 3936–3947, 2018.

[32] R. Moore, *Interval Analysis*, Prentice-Hall, Upper Saddle River, NJ, USA, 1966.

[33] G. Alefeld and J. Herzberger, *Introduction to Interval Computations*, Academic Press, Cambridge, MA, USA, 1983.

[34] L. V. Kolev, *Interval Methods for Circuit Analysis*, World Scientific, Singapore, 1993.

[35] J. Michel and F. Schwartz, "Analogue circuit sizing method using interval analysis," in *Proceedings of the 2008 Joint 6th International IEEE Northeast Workshop on Circuits and Systems and TAISA Conference*, pp. 331–334, Montreal, Canada, June 2008.

[36] N. Anselmi, L. Manica, P. Rocca, and A. Massa, "Tolerance analysis of antenna arrays through interval arithmetic," *IEEE Transactions on Antennas and Propagation*, vol. 61, no. 11, pp. 5496–5507, 2013.

[37] P. Rocca, M. Carlin, and A. Massa, "Imaging weak scatterers by means of an innovative inverse scattering technique based

on the interval analysis," in *Proceedings of the 2012 6th European Conference on Antennas and Propagation (EUCAP)*, pp. 1139-1140, Prague, Czech Republic, March 2012.

[38] M. Carlin, P. Rocca, G. Oliveri, and A. Massa, "Interval analysis as applied to inverse scattering," in *Proceedings of the 2012 IEEE International Symposium on Antennas and Propagation*, Chicago, IL, USA, July 2012.

[39] L. Manica, P. Rocca, M. Salucci, M. Carlin, and A. Massa, "Scattering data inversion through interval analysis under rytov approximation," in *Proceedings of the 7th European Conference on Antennas and Propagation (EuCAP)*, pp. 82–85, Gothenburg, Sweden, April 2013.